

# Analysis of Feature Visibility in Non-Line-of-Sight Measurements

Xiaochun Liu

xliu669@wisc.edu

Sebastian Bauer

sbauer8@wisc.edu

Andreas Velten\*

velten@gmail.com

University of Wisconsin – Madison

## Abstract

We formulate an equation describing a general Non-line-of-sight (NLOS) imaging measurement and analyze the properties of the measurement in the Fourier domain regarding the spatial frequencies of the scene it encodes. We conclude that for a relay wall with finite size, certain scene configurations and features are not detectable in an NLOS measurement. We then provide experimental examples of invisible scene features and their reconstructions, as well as a set of example scenes that lead to an ill-posed NLOS imaging problem.

## 1. Introduction

Time of flight non-line-of-sight (NLOS) imaging uses fast illumination sources and detectors to probe multi-bounce light transport of scenes not directly visible to the observer (Figure 2). An illumination source illuminates points  $p_i$  on a relay surface with short pulses and captures light returning from the scene to points  $p_d$  on the relay wall. By solving the inverse light transport problem from those NLOS measurements, the invisible 3D space can be reconstructed. We refer to this type of time of flight (time-resolved) NLOS measurement simply as NLOS measurement.

Different inverse methods have been developed to reconstruct hidden scenes from the time of flight data such as filtered backprojection [18, 7, 3, 10], similar to backprojection methods used in computed tomography problems. Other methods formulate the light transport in the hidden scene as a linear matrix operator and solve a matrix inverse problem to reconstruct the scene through an optimization framework [9]. More recently, O’Toole et al. showed that for confocal datasets (see Fig. 2 **a**; on the other hand, **b** shows the non-confocal NLOS measurement) the forward integral can be simplified to a convolution operator. Thus the inverse process can be expressed as a deconvolution problem and solved efficiently [13]. Other methods perform the reconstruction using subsets of the measurement data such as the

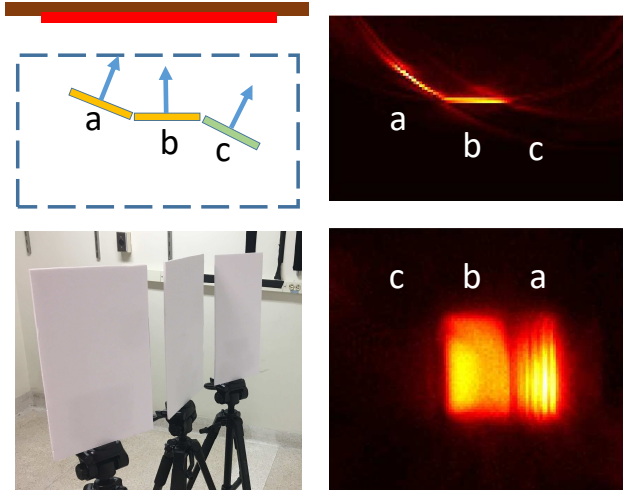


**Figure 1. Three patches rotation example.** Experimental reconstruction of a scene containing three patches denoted by **a**, **b**, **c**. Patches **a** and **c** are parallel but the latter one’s surface normal vector does not point towards the NLOS relay wall and the patch does not appear in the reconstruction shown on the right. The first row stands for the top view and the second row for the front view. The explanation for this astonishing effect will be developed in the main text, see Sec. 6.2, and also Fig. 8 for a graphical explanation.

first returned photon [16], or parameterizing the reconstruction as a set of planes [14]. Other reconstruction techniques are described in [19, 17]. Some existing approaches even model partial occlusions within the hidden scene, e.g., [8]. The findings about reconstruction techniques developed for NLOS imaging have also been transferred to acoustic imaging around corners [11].

In this work, we aim to provide a generic description for direct bounce (3rd bounce) NLOS measurements and show how much information they encode and how this affects practical NLOS imaging problems.

Consider the NLOS reconstruction shown in Figure 1. It contains three very similar patches that only vary slightly in orientation and have different positions in the reconstruction space. Yet while two of the patches are reconstructed

clearly and accurately, the third is completely missing from the reconstruction. A closer inspection of prior published results reveals that similar artifacts are seen in reconstructions using a variety of diverse reconstruction methods. Surfaces with certain normal vectors are missing in the reconstruction or scenes with simple surfaces are chosen to avoid the problem. The main purpose of this work is to explain this phenomenon.

As we show below, any NLOS measurement can be expressed as an integral operator known in the literature as elliptical Radon integral. We analyze this measurement function in the Fourier domain and show that a significant part of the measurement space is not accessed by the NLOS measurement and thus represents a null space for NLOS reconstruction. Finally, we investigate the Fourier domain representations of common scenes and scene features to identify features that fall into the null space and cannot be reconstructed. Because our analysis involves a generic description of the NLOS measurement, it is independent of the reconstruction algorithm used. We expect our findings will inform inverse solution design and future NLOS reconstruction methods.

## 2. Related Work

Statements of the properties of NLOS reconstructions are sometimes included with a presentation of reconstruction algorithms. For example, the available resolution has been analyzed [3, 13]. Since the underlying mathematical forward model shares a similar root as the computed tomography problem (Radon integral), much more extensive work on this problem is available through related problems. Radon integrals have been studied for their applications in ultrasound imaging and medical computed tomographies [20, 15, 12]. The effect of a finite-sized sampling aperture is similar to the missing cones problem that has been the subject of extensive research in medical computed tomography (CT) imaging [5, 1].

Radon integrals can be categorized into classical Radon integral (planar), spherical Radon transform (SRT) and elliptical (ellipsoid) Radon transform (ERT). The planar Radon transform with its high dimensional model [4] is well known in the CT field. The spherical Radon transform (SRT) with its inverse solution design can be found in [20, 15]. A similar inverse formula for the confocal measurement setup applies for the SRT model used in ultrasound [15] and NLOS imaging [13]. The elliptical Radon transform (ERT) has been studied by Moon et al. [12]. An inverse to the ERT was proposed in [6] and is similar to (but not the same as) the NLOS non-confocal filtered backprojection method [18, 7, 3].

## 3. Contributions

Our contributions in this work are as follows:

- We formulate a generic measurement equation for time of flight NLOS imaging with limited visible wall size and analyze the information sampled by the NLOS capturing process in the spatial frequency domain. This allows us to make statements about visible and invisible features in the measurement space that are independent of all linear deterministic reconstruction methods.
- Based on our model, we analyze some commonly used scene features resulting in a simple rule to predict feature visibility for NLOS imaging.
- We confirm our conclusion with experimental data.
- To further demonstrate the nature of the missing data, we also provide an exemplary *challenge scene*. Scenes like these lead to identical NLOS measurement datasets despite having different scene geometries.

## 4. NLOS imaging problem

In this section, we are going to provide basic mathematical tools for modeling the NLOS imaging problem in a general way by introducing the NLOS measurement function and its properties. Then we introduce the concept of limited aperture NLOS imaging which results in an incomplete measurement space. This incomplete measurement space is essential for the next section dealing with our measurement analysis in the spatial Fourier domain in Sec. 5.

### 4.1. NLOS Measurement Function

The NLOS measurement scenarios are illustrated in Figure 2 on the left, and two measurement setups are shown in the subfigures **a** and **b**. In an NLOS measurement, the scene is illuminated from a point  $p_i$  (illumination position) and light returning from the scene is recorded at a detection point  $p_d$  (detection position) after a certain time interval  $t$ . Both  $p_i$  and  $p_d$  are within the finite area of the relay wall that we call the NLOS sampling aperture. In practice, this sampling aperture is bounded by the limited field of view because of the remote detection.

We use  $f(\mathbf{p})$  to represent the unknown 3D scene we would like to recover. Here  $f(\mathbf{p})$  is a function of the vector  $\mathbf{p} = (x, y, z)$  storing the reflectance values in space. We assume uniform scattering, thus the reflectance value is angle independent. The function  $g$  represents one single time response measurement at illumination position  $p_i$  and detection position  $p_d$ . Thus, each time resolved measurement  $g(p_i, p_d, t)$  is a function of illumination position  $p_i$ , detection position  $p_d$  and time  $t$ . The NLOS measurement is made up of a set of detection positions (detection grid) from

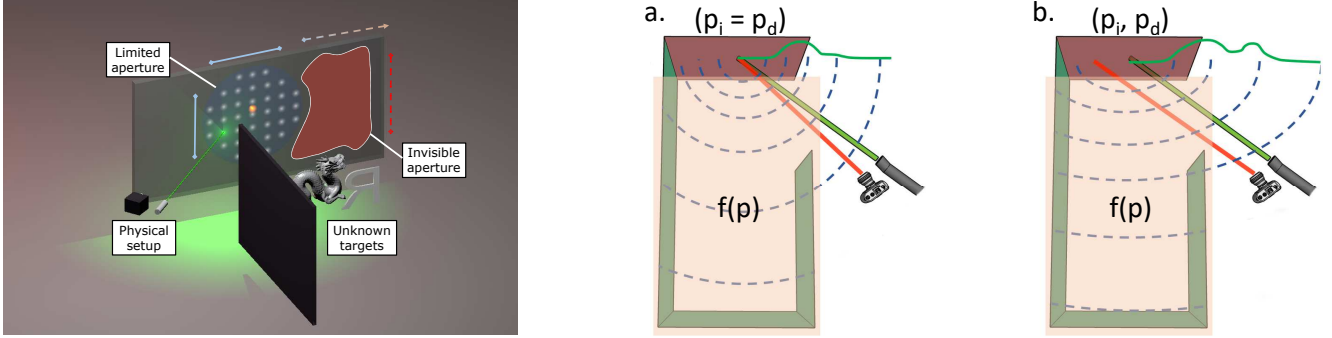


**Figure 2. Illustration of a NLOS measurement:** The panels a and b show two popular NLOS measurement setups. Subfigure a shows the confocal measurement which means the illumination and detection point are co-located, while b shows the non-confocal measurement. The green curves in a and b sketch the acquired time responses, i.e., the integration of reflecting scene features along each circle (confocal case) or ellipse (non-confocal case).

a single or multiple subsequent point illuminations on the wall. We use  $G = \{g_1, g_2, g_3, \dots, g_n\}$  to represent all measurements. We focus on illustrating the transformation from  $f(\mathbf{p})$  to one single measurement  $g(\mathbf{p}_i, \mathbf{p}_d, t)$  first. Then it is straightforward to understand the transformation from  $f(\mathbf{p})$  to the entire measurement set  $G$ . Subfigures a and b of Figure 2 represent the confocal and non-confocal measurement setups. Since the non-confocal case is the more general version of NLOS measurement, we start our forward modeling from the non-confocal measurement.

We can use an integral operator  $A : f(\mathbf{p}) \rightarrow g(\mathbf{p}_i, \mathbf{p}_d, t)$  to represent the linear transform from the unknown function  $f(\mathbf{p})$  to a temporal measurement at given detection and illumination positions and time  $g(\mathbf{p}_i, \mathbf{p}_d, t)$ . This results in the NLOS measurement equation:

$$g(\mathbf{p}_i, \mathbf{p}_d, t) = \int_{\mathbb{R}^3} \Upsilon(d_i, d_d) \cdot \delta(d_i + d_d - t \cdot c) \cdot f(\mathbf{p}) d\mathbf{p}. \quad (1)$$

In the literature, this integral is often referred to as the Elliptical Radon Transform (ERT). The delta function kernel in this equation describes the geometry of the integration, and  $c$  denotes the speed of light. To simplify notation, we use the distance terms  $d_i = |\mathbf{p} - \mathbf{p}_i|$  and  $d_d = |\mathbf{p} - \mathbf{p}_d|$  which represent the distances between the integral variable  $\mathbf{p}$  and illumination/detection position, respectively. The term  $\Upsilon(d_i, d_d)$  stands for the intensity drop-off associated with distances traveled by the light. This intensity term is normally not included in the ERT, however we add it in this treatment as it is needed to correctly model the physical measurement process. The integration (1) can be performed for an entire family of thin ellipsoid surfaces having different foci  $\mathbf{p}_i$  and  $\mathbf{p}_d$ .

Any set of NLOS measurements made from locations within the NLOS aperture area can be expressed as a set of these measurement functions. The integral in Equation (1) is difficult to treat analytically because of non-constant cur-

vatures. Therefore we also consider two simplified scenarios. If we allow only measurements where  $\mathbf{p}_i = \mathbf{p}_d$ , we obtain the confocal NLOS measurement (Figure 2 a)

$$g(\mathbf{p}_i, \mathbf{p}_i, t) = \int_{\mathbb{R}^3} \Upsilon(d_i) \cdot \delta(2 \cdot d_i - t \cdot c) \cdot f(\mathbf{p}) d\mathbf{p}. \quad (2)$$

This integral without intensity term  $\Upsilon(d_i)$  is also known in the literature as the spherical Radon transform (SRT) [20, 15].

Another useful tool to approximate the measurement function is to locally replace the elliptical integral by integrals over planes that are tangential to the ellipsoids. This refers to a zoom-in version of the integration at a local volume. Since the integral is a linear operator, the measurement can be represented as superposition of all individual inputs (linearity). Then for each individual input, the local integral version can be approximated by the planar integral. This means:

We linearize the unknown 3D function  $f(\mathbf{p})$  by a summation of local functions  $f_1, f_2, \dots, f_n$  which store the features representing the 3D image. Each local function represents a local pattern within cube volumes at different positions such that each subspace contains only small sections of the ellipsoids. Each ellipsoid  $g(\mathbf{p}_i, \mathbf{p}_i, t)$  can within that subspace be approximated by planes  $g'(t, \theta, \phi)$  where the planar angles  $\theta$  and  $\phi$  are such that the plane normal vector points to the center of the ellipsoid and  $t$  is proportional to twice the distance between the ellipsoid center and the plane. In polar coordinates, this yields

$$g'_{(\theta, \phi)}(t) = \iiint_{-\infty}^{\infty} f(x, y, z) \cdot \delta(\sin \theta \cos \phi x + \sin \theta \sin \phi y + \cos \theta z - t \cdot c) dx dy dz. \quad (3)$$

This planar approximation has been described before in [18, 7] to approximate the NLOS imaging result from non-confocal streak camera measurements. It is also similar in

nature to the approximation made when using a piecewise definition of a locally varying point spread function as is often done in point spread function deconvolution problems.

Above all, we provide the basic tools for describing the NLOS forward model which we are going to use in Section 5. There, we provide our main tools to analyze the incomplete measurement space effect. Our idea is to mimic the imaging system by illustrating the information content in the Fourier domain by the modulation transfer function (MTF) dependent on a given limited aperture.

## 5. NLOS Measurements in the Fourier domain

A complete description of a measurement of a section of  $f(\mathbf{p})$  can be described as the set of all  $g(\mathbf{p}_i, \mathbf{p}_d, t)$  for which  $\mathbf{p}_i$  and  $\mathbf{p}_d$  are in the NLOS aperture plane and  $t$  is such that the measurement ellipsoid goes through  $f(\mathbf{p})$ . To obtain insight into the patterns in the scene that are sampled by this measurement, we want to analyze them in the Fourier domain. The Fourier domain NLOS measurement function can be understood as a Modulation Transfer Function (MTF) of NLOS imaging.

For the planar Radon transform (PRT, Equation (3)), the Fourier transform of  $g'$  can be computed analytically using the projection-slice theorem.

### 5.1. Projection slice theorem

The projection slice theorem (PST) is well-known and widely used in the area of computed tomography and other fields. We will give a short explanation of the 2D version here; the 3D version is shown in the supplemental document. The PST provides an elegant tool for using projections (i.e., integrals) along parallel lines of an unknown 2D scene: it shows that the 1D Fourier transform of such projections actually represents one line through the origin of the 2D Fourier spectrum of the unknown scene. Repeating the process for different projection angles provides the missing lines; scene reconstruction is then easily achieved by inverse 2D FT.

The unknown 2D function is denoted by  $f(x, y)$ . Let us first assume that the projection angle  $\theta$  is zero. The projection dependent on the displacement  $u$  with respect to the origin and vertically to the projection direction is then given by [2]

$$\begin{aligned} f_{\text{proj}}(u, \theta = 0) &= \iint f(x, y) \delta(x - u) dx dy \\ &= \int f(u, y) dy. \end{aligned}$$

Performing the 1D Fourier transform with respect to  $u$

yields

$$\begin{aligned} \mathcal{F}_u\{f_{\text{proj}}(u, 0)\} &= \iint f(u, y) e^{-j2\pi f_u u} du dy \\ &= \iint f(x, y) e^{-j2\pi f_x x} dx dy \\ &= \iint f(x, y) e^{-j2\pi(f_x x + f_y y)} dx dy \Big|_{f_y=0}. \end{aligned} \quad (4)$$

This corresponds to the 2D Fourier transform of the unknown function  $f(x, y)$  at the line with  $f_y = 0$ . Repeating the projection with different angles  $\theta$  results in the corresponding line of the 2D Fourier transform; note that rotation in the spatial domain corresponds to a rotation by the same angle in the frequency domain. By considering all angles  $\theta$  from 0 to  $2\pi$  and adding all Fourier spectrum lines, the full function  $f(x, y)$  can then be reconstructed by inverse 2D Fourier transform. It is advisable to apply a high pass filter before the inverse Fourier transform, as high frequencies are underrepresented because of the spectral lines meeting in the origin, but diverging for higher frequencies, which means that there is less information available for these frequencies. This is called *filtered backprojection* [4].

In the 3D case, the projection along parallel planes and subsequent 1D Fourier transform of the calculated (scalar) projection values for each plane provides one line of the 3D spectrum of  $f(\mathbf{p})$ . Rotating the projection planes about the origin provides the spectrum along all lines through the origin. See the supplementary document for details.

### 5.2. Local Fourier cone

The left part of Figure 5 shows the measurement for two cases where the illumination and detection points are co-located at  $a$  or  $b$  at either side of the relay wall. In the middle of that figure, we can see that the collected time response for those two cases are projections along directions with angles  $\Theta_1$  or  $\Theta_2$  with respect to the relay wall. The exact projections are performed along ellipsoids; however, we approximate these as planes. As it is shown on the right of Figure 5, the Fourier slice theorem states that the 1D Fourier transform of the projections of the scene along parallel planes at angle  $\Theta$  in the primal domain is equal to a slice at angle  $\Theta$  in the 2D Fourier spectrum of the scene. To create a cone we then simply draw the corresponding lines for all accessible points on the relay wall. By using a limited size relay wall, the black part of the spectrum is not contained in any measurements.

**Null space and cone variation:** As shown in Fig. 3, given the same size of the limited aperture, the closer the considered volume is to the sampling aperture, the larger the visible angle range of this cone is (compared with position 1 and position 4 in Fig. 3). Moreover, offset with regard to the center of the aperture also tilts this sampling

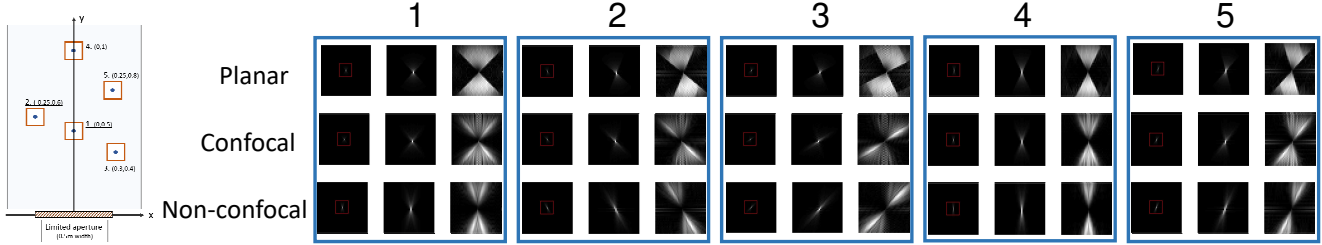


Figure 3. **Local Measurement MTF:** Fourier domain representations of the NLOS Measurement Function for five points in the unknown geometry. The left graphic represents the geometric setup. We construct a half meter limited aperture with five volumes of interest varying in depth and horizontal offset. The panels show the measurement function for all points for the different models. Planar corresponds to the PRT, confocal to the SRT, and non-confocal to the SRT. For each point, the first column shows the computed patterns, the middle column shows the same pattern zoomed in, and the right column shows the zoomed in pattern after correcting for the lower values at higher frequencies to enhance visualization.

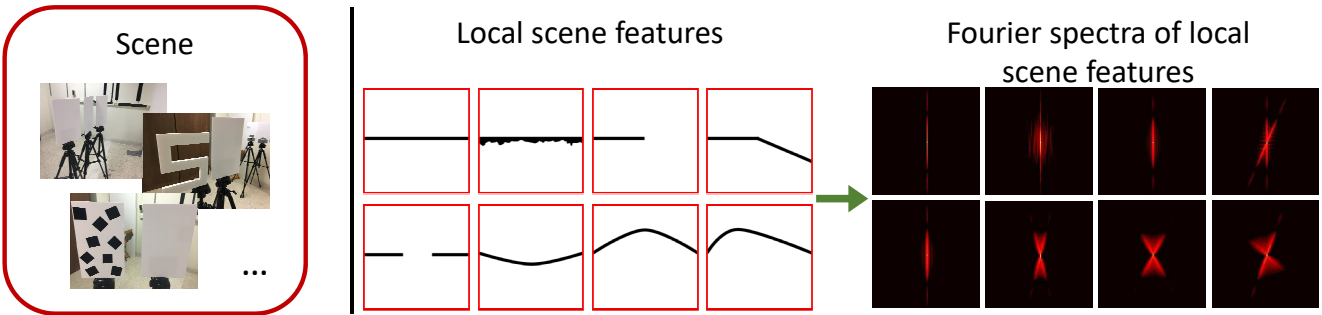


Figure 4. **Local scene features:** This figure shows a set of common NLOS scene features in the red boxes and their Fourier transforms. Rotating of the features simply corresponds to rotating by the same angle in the Fourier domain. The patterns are (top left to bottom right) a smooth planar surface, a rough planar surface, the edge of a planar surface, a corner between two surfaces, a gap in a planar surface, a convex curved surface, and two concave curved surfaces. The spectrum of a planar surface is a line. Roughness, curvature, and edges result in spectra that also cover other regions of the Fourier space.

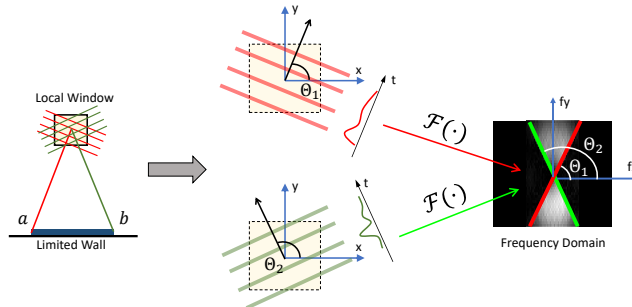


Figure 5. Fourier slice theorem and cone generation.

cone in the Fourier domain (refer to positions 2, 3 and 5 in Figure 3). Overall, things outside this cone will never be sampled in the Fourier domain by the limited aperture unless the aperture size is increased. This means that, e.g., a wall placed perpendicularly to the relay wall has a Fourier transform which, apart from the DC value at frequency 0, will fully vanish in the missing cone and cannot be seen in any reconstruction not accounting for the missing cone.

**Model validity:** To verify the model validity, we perform a computation for planar, confocal and non-confocal

measurement (fixed illumination as one focus at the center) with the same limited aperture. With an acceptable error in the discrete model, we can see from Fig. 3 that the local planar model gives a good boundary estimation for the confocal and non-confocal cases. Notice that we fixed one focus  $p_i$  in the non-confocal case resulting in a more narrow MTF pattern. By moving the non-confocal illumination spot, this narrow cone slightly rotates which could achieve a similar angle coverage in the confocal measurement.

## 6. Measurement of scene features

**Local scene features:** To use the proposed analysis, we need to decompose any complicated NLOS imaging scenes into simple features such as planes etc. This is shown in Fig. 4, which also displays their Fourier spectra which defines their reconstructability, cf. Fig. 5 and the following paragraph. Most of the simple features can be represented as a thin surface with different roughness level as well as edge like discontinuity patterns and curvatures. Rotation of the patterns in space simply corresponds to the same rotation in the Fourier domain.

**MTF with scene features:** To assess visibility of the

targets we have to consider the overlap between the target spectra and the MTF sampling cone. This will be shown illustratively in the results, see Section 6.2. Note that the most valuable information is encoded in the high frequency components of the cone. The center of the cone is at the origin and thus samples the low spatial frequencies. The high frequency components far away from the origin are necessary to create high resolution reconstructions.

**Limited aperture ill-posed example:** Limited aperture NLOS imaging with arbitrary targets should be viewed as an ill-posed problem. Consider a simple patch with different rotation angles with respect to the limited aperture. Once it is facing the sampling aperture and located at its center, its local Fourier spectrum is optimally covered by the MTF Fourier cone. However, when the patch pattern rotates, its Fourier pattern also rotates by the same angle. Once it rotates outside the angle covered by each local cone, the recorded information only includes the origin in the Fourier plane, corresponding to a constant or zero spatial frequency. See the experiments in Sec. 6.2 for an illustration of this effect. Overall, this means we can still see that a structure is there (after all, there is light coming back) but we cannot actually uniquely reconstruct it. On the other hand, a local pattern containing high spatial frequency contents like edges or surface roughness has a much broader spectrum and at least part of it always overlaps with the measurement cone making it at least partially reconstructible.

**Rule-of-thumb criterion:** From this, we can also derive a simple rule for visibility of scene patches. Since a planar scene segment is represented by a line through the origin in the Fourier domain, the segment will be completely visible if the line lies within the sampled cone, and invisible if it is at an angle outside the cone. **In the primal domain this means that a segment is only visible when its normal vector points toward the relay wall.**

Overall, for NLOS imaging scenarios, more higher spatial frequency components of unknown targets subsequently result in more fluctuations in the temporal measurements. For this reason, they lead to a higher chance to actually see the target by using all deterministic linear inverse solutions from a limited aperture.

## 6.1. Completely invisible feature example

To provide further evidence for the existence of a universal, reconstruction independent null-space, we provide a set of example scenes that are simple enough to be treated analytically for a confocal measurement set. To do this, we replace  $f(\mathbf{p})$  by specific functions to represent the scene features inside the integral measurement equations (1) and (2). To simplify the calculation, we consider only a two dimensional scenario of a confocal NLOS measurement.

**Smooth wall example (Challenge scene):** As it is

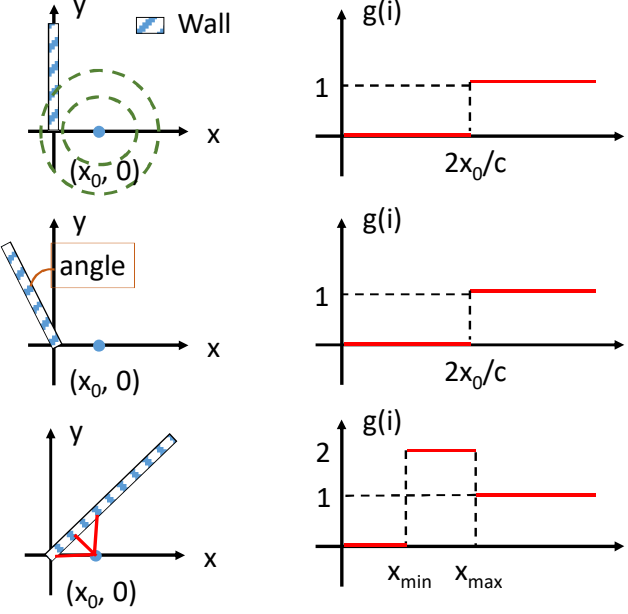


Figure 6. Three wall examples. The first column represents the geometry, the second column stands for the measurement  $g(i)$  after the intensity correction from  $t(i)$ . The scenes in the first two rows lead to identical captured data.

shown in Figure 6, the unknown target is a smooth wall at an angle to the relay wall described by  $\delta(\cos(\theta)x - \sin(\theta)y)$  for  $y \geq 0$ . For confocal NLOS measurements, our illumination and detection are co-located at the  $x$ -axis meaning that  $\mathbf{p}_i = \mathbf{p}_d = (x_0, 0)$ ,  $x_0 \geq 0$ . Since the distance correction simply amplifies the signal at each given time index  $i$ , we use the notation  $C(i)$  to represent this correction term. We use the term  $g(i)$  to represent the reflectance integration at each time index  $i$ . By plugging this special function into the Radon integral, we obtain the following equation:

$$g(i) = C(i) \cdot \int_0^\infty \int_{-\infty}^\infty \delta(\cos(\theta)x - \sin(\theta)y) \cdot \delta((x - x_0)^2 + y^2 - (\frac{c \cdot i}{2})^2) dx dy. \quad (5)$$

By performing the distance correction  $C(i)$  to account for the distortion from the intensity drop off, the measurement  $g(i)$  simply represents a set of reflectance integrals in the unknown space.

Using the fact that  $\delta(\cos(\theta)x - \sin(\theta)y)$  is only 1 for  $\cos(\theta)x = \sin(\theta)y$ , we can replace  $x$  by  $y \tan(\theta)$  and further simplify the equation by getting rid of integral variable  $x$  as follows:

$$g(i) = C(i) \cdot \int_0^\infty \delta((\tan(\theta)y - x_0)^2 + y^2 - (\frac{c \cdot i}{2})^2) dy \quad (6)$$

From this equation, it is clear to see that the final mea-

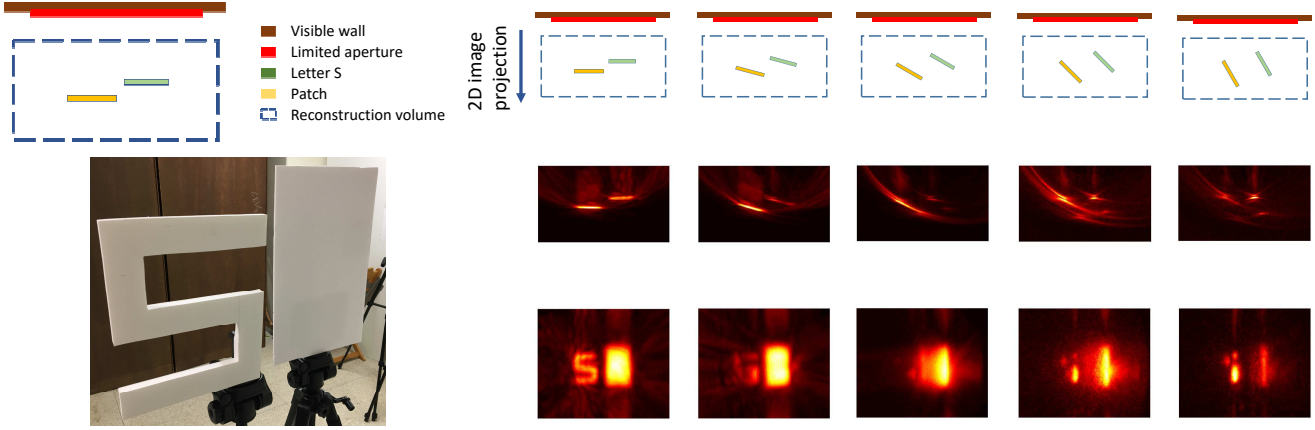


**Figure 7. Simple letter S and rectangle patch rotation experiments** The first row represents the schematic of the setup including the entire visible wall, limited aperture, targets (letter S and patch) as well as reconstruction volume. The next two rows show the maximum projection along the depth dimension, thus a 2D bird view and 2D front view are provided. For clear illustration, we present results using two-color (bright and dark view). The thickness of the letter S and the rectangular patch approximately equals 5 cm and 0.5 cm. As the angle increases, the ill-posed effect becomes more obvious, and certain features are missing in the measurement space and therefore cannot be resolved by the reconstruction

surement can be viewed as a sum of 1 or 0 at any given time index  $\hat{i}$  when the kernel inside the integral  $(\tan(\theta)y - x_0)^2 + y^2 - (\frac{c\hat{i}}{2})^2 = 0$ . This parabolic equation may have zero, one or two solutions with fixed  $\theta, x_0$ . This means the final measurement  $g$  may be 0, 1 or 2 at any given time index. A simple observation is that, once the wall reaches angle  $\theta = \pi/2$ , the value of the integral is the same for all  $p_i = (x_0, 0)$ ,  $x_0 \geq 0$  on the aperture line. The signal  $g$  with different wall rotation angles is shown in Figure 6. Thus, all scenes with walls at angles above  $\theta = \pi/2$  result in the same NLOS data and are thus not distinguishable without any prior constraints. Extending this treatment to a 3D space results in more complex equations and is therefore less instructive. It is subject of further study.

## 6.2. Experiments

We perform two experiments of ill-posed scenarios which are first predicted by our proposed local cone model. For the reconstruction process, we choose a filtered back-projection [18, 7, 3] without thresholding process. For visualization, we choose the maximum projection along the depth dimension in the front view. Also, we provide a maximum projection for the bird view.

In Figure 7 we show a rotating letter S and planar patch example. As shown in the result, the simple patch pattern is completely resolvable when facing directly to the limited aperture. In this situation all patch normals are pointing at the relay wall aperture. As the targets rotate, normals start pointing past the aperture and the planes start to disappear. Not all target patches disappear simultaneously due to the local variations in Fourier cone discussed above. Eventually, all patch normals point outside the aperture and the

entire targets are outside the Fourier cone. We can only resolve the high spatial frequency pattern at edges in the final reconstruction.

Another three patches example was already shown in Figure 1. Having now the theoretical tools at hand, we see in Fig. 8 that both patches **a** and **c** have the same magnitude spectrum, but because of the spatially dependent measurement cone, only the offset of patch **c** is captured. In the reconstruction, this patch is therefore almost entirely invisible.

## 7. Discussion and Conclusion

Using a limited aperture NLOS sampling measurement and a simple patch target, the following statements can be made based on our presented model for non-resolvable scene features.

- Consider a patch that is directly facing to and located inside the sampling aperture window. The closer it is to the sampling wall, the more resolvable it becomes and the reconstruction quality increases.
- Target surfaces offset or rotated in the unknown volume are only visible if their normal vector points to the relay wall aperture.
- While it is not possible to reconstruct missing patches, we can detect if missing patches exist as they still reflect light.
- When comparing reconstruction quality among different inverse methods, it is important to be aware of how much information is available in the measurement

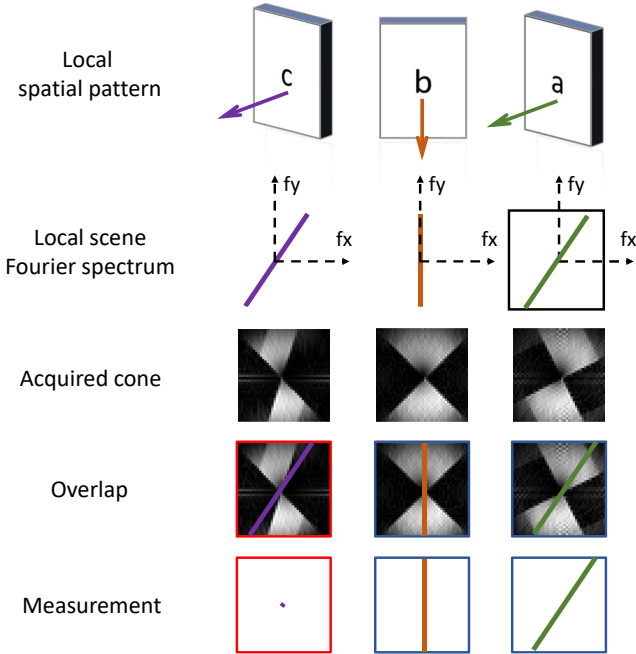


**Figure 8. Explanation of the missing feature in Fig. 1** The measurement cone is shown as gray area and illustrates the part of the Fourier spectrum that is actually acquired by NLOS measurements. It varies with the position in the 3D space that is to be reconstructed. Both patches **a** and **c** of the scene are oriented the same way; the spatial shift just corresponds to a phase shift in the Fourier domain, but not in a change of the magnitude spectrum. This means both patches have the same magnitude spectrum, but due to the fact that the measurement cone is different at their respective positions, the measurement of patch **c** only captures the offset and not the rest of the spectrum. For this reason, this patch cannot be reconstructed.

space. This means future datasets and research should specify the sampling aperture/target location as well as sampling aperture size.

Our statements apply to any NLOS measurement that involves only the direct (3rd bounce) light from the hidden scene. Missing features may be reconstructed by algorithms by making use of higher order bounces, or missing information may be filled in using priors. This hole filling solution is different from deblurring and de-noising tasks common in imaging. The modulation transfer functions we derive are zero outside the Fourier cone (as opposed to just being very small like a Gaussian). This means deblurring methods based on deconvolution will fail, even for noiseless data.

The limited aperture NLOS scenario is essential to be understood for future inverse method design. All the deterministic linear inverse methods can only recover the scene features which are contained in the limited measurement space. Overall, based on our local MTF sampling cone model, it is easy to see this limited aperture problem. By allowing any targets around the corner, some scene features may not be

well represented, or completely missing in the incomplete measurement space. Future inverse method design should go beyond deterministic inverse methods by adding prior constraints to the inverse model to specifically account for this ill-posed limited aperture problem.

In this work we provide only an approximate analytical model that we back up with numerical computations of the exact functions. An exact analytical expression for the Fourier cone is subject of further research.

**Acknowledgment** This work was funded by DARPA through the DARPA REVEAL project (HR0011-16-C-0025), the NASA NIAC program, and the AFOSR through the Young Investigator Program (FA9550-15-1-0208), and the DURIP program (FA9550-18-1-0409).

## References

- [1] M. Benning, C. Brune, M. J. Lagerwerf, and C.-B. Schönlieb. TGV sinogram inpainting for limited angle tomography. In *Technical Report*. University of Cambridge, 2015. [2](#)
- [2] J. Beyerer, F. P. León, and C. Frese. *Machine vision: Automated visual inspection: Theory, practice and applications*. Springer, 2015. [4](#)
- [3] M. Buttafava, J. Zeman, A. Tosi, K. Eliceiri, and A. Velten. Non-line-of-sight imaging using a time-gated single photon avalanche diode. *Optics Express*, 23(16):20997–21011, 2015. [1, 2, 7](#)
- [4] S. R. Deans. *The Radon transform and some of its applications*. Courier Corporation, 2007. [2, 4](#)
- [5] A. H. Delaney and Y. Bresler. Globally convergent edge-preserving regularization: an application to limited-angle tomography. *IEEE Transactions on Image Processing*, 7(2):204–221, 1998. [2](#)
- [6] R. Gouia-Zarrad and G. Ambartsoumian. Approximate inversion algorithm of the elliptical Radon transform. In *Mechatronics and its Applications (ISMA), 2012 8th International Symposium on*, pages 1–4. IEEE, 2012. [2](#)
- [7] O. Gupta, T. Willwacher, A. Velten, A. Veeraraghavan, and R. Raskar. Reconstruction of hidden 3D shapes using diffuse reflections. *Optics Express*, 20(17):19096–108, Aug 2012. [1, 2, 3, 7](#)
- [8] F. Heide, M. O’Toole, K. Zang, D. Lindell, S. Diamond, and G. Wetzstein. Non-line-of-sight imaging with partial occluders and surface normals. *ACM Trans. Graph.*, 2019. [1](#)
- [9] F. Heide, L. Xiao, W. Heidrich, and M. B. Hullin. Diffuse mirrors: 3D reconstruction from diffuse indirect illumination using inexpensive time-of-flight sensors. In *Proceedings of the IEEE Conference on Computer Vision and Pattern Recognition*, pages 3222–3229, 2014. [1](#)
- [10] M. La Manna, F. Kine, E. Breitbach, J. Jackson, T. Sultan, and A. Velten. Error backprojection algorithms for non-line-of-sight imaging. *IEEE Transactions on Pattern Analysis and Machine Intelligence*, 2018. [1](#)
- [11] D. B. Lindell, G. Wetzstein, and V. Koltun. Beyond volumetric albedo a surface optimization framework for non-line-of-

- sight imaging. In *Proceedings of the IEEE Conference on Computer Vision and Pattern Recognition*, 2019. 1
- [12] S. Moon. On the determination of a function from an elliptical Radon transform. *Journal of Mathematical Analysis and Applications*, 416(2):724–734, 2014. 2
  - [13] M. O’Toole, D. B. Lindell, and G. Wetzstein. Confocal non-line-of-sight imaging based on the light-cone transform. *Nature*, 555(7696):338, 2018. 1, 2
  - [14] A. K. Pedireddla, M. Buttafava, A. Tosi, O. Cossairt, and A. Veeraraghavan. Reconstructing rooms using photon echoes: A plane based model and reconstruction algorithm for looking around the corner. In *2017 IEEE International Conference on Computational Photography (ICCP)*. IEEE, 2017. 1
  - [15] J. Tasinkevych and I. Trots. Circular Radon transform inversion technique in synthetic aperture ultrasound imaging: an ultrasound phantom evaluation. *Archives of Acoustics*, 39(4):569–582, 2015. 2, 3
  - [16] C.-Y. Tsai, K. N. Kutulakos, S. G. Narasimhan, and A. C. Sankaranarayanan. The geometry of first-returning photons for non-line-of-sight imaging. In *IEEE International Conference on Computer Vision and Pattern Recognition (CVPR)*, 2017. 1
  - [17] C.-Y. Tsai, A. Sankaranarayanan, and I. Gkioulekas. Beyond volumetric albedo a surface optimization framework for non-line-of-sight imaging. In *Proceedings of the IEEE Conference on Computer Vision and Pattern Recognition*, 2019. 1
  - [18] A. Velten, T. Willwacher, O. Gupta, A. Veeraraghavan, M. G. Bawendi, and R. Raskar. Recovering three-dimensional shape around a corner using ultrafast time-of-flight imaging. *Nature Communications*, 3:745, 2012. 1, 2, 3, 7
  - [19] S. Xin, S. Nousias, K. Kutulakos, A. Sankaranarayanan, S. Narasimhan, and I. Gkioulekas. A theory of fermat paths for non-line-of-sight shape reconstruction. In *Proceedings of the IEEE Conference on Computer Vision and Pattern Recognition*, 2019. 1
  - [20] M. Xu and L. V. Wang. Universal back-projection algorithm for photoacoustic computed tomography. *Physical Review E*, 71(1):016706, 2005. 2, 3